3D atomic imaging of low-coordinated active sites in a solid-state dealloyed hierarchical nanoporous gold

Chunyang Wang[1,3,†], Hongyang Liu[1,†] , Huichao Duan[1,2,†], Zhenwei Li[1,2], Panlin Zeng[1,2], Peichao Zou[3], Xuelu Wang[1,2], Hengqiang Ye[1], Huolin L. Xin[3,*], Kui Du[1,*]

[1]Shenyang National Laboratory for Materials Science, Institute of Metal Research, Chinese Academy of Sciences, Shenyang 110016, China

[2]School of Materials Science and Engineering, University of Science and Technology of China, Shenyang 110016, China

[3]Department of Physics and Astronomy, University of California, Irvine, CA 92697, United States

*Corresponding author. E-mail: huolinx@uci.edu or kuidu@imr.ac.cn

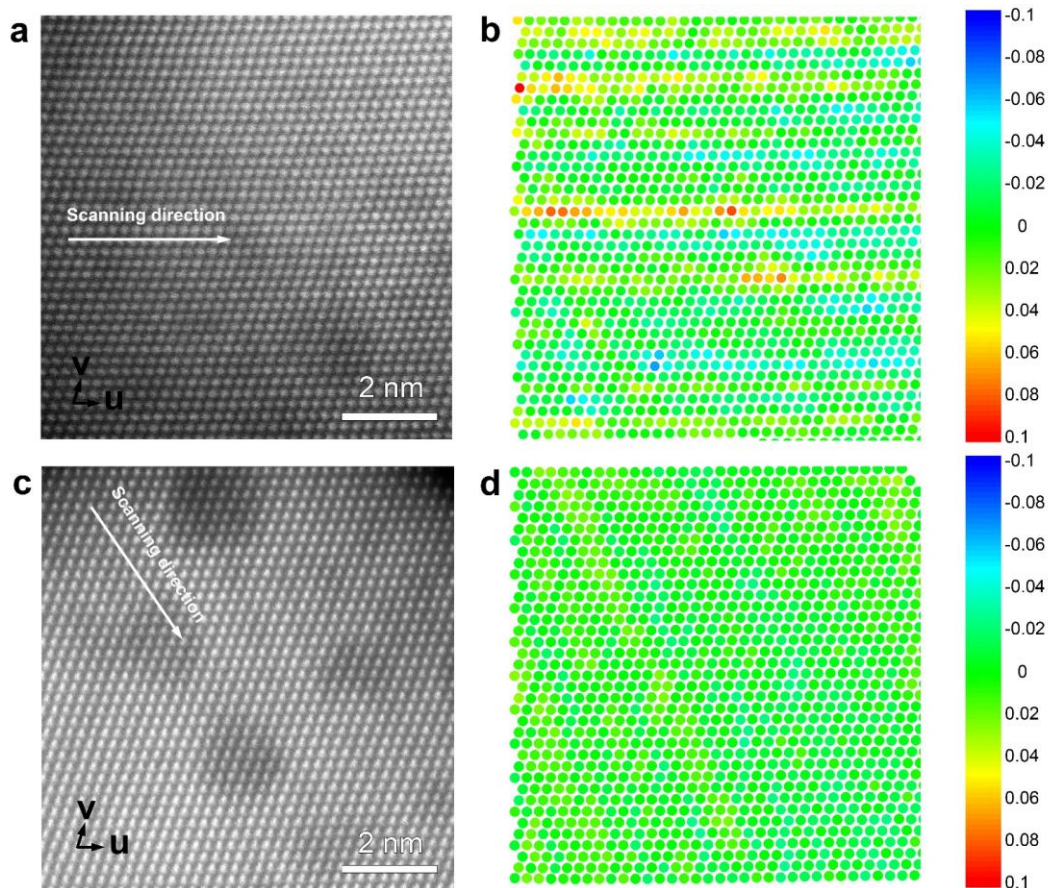[†]These authors contribute equally to this work.

Fig. S1. Comparison of image distortion introduced during scanning in aberration corrected-TEM without and with the panel cooling system. a,b) Image distortion in HAADF-STEM images obtained by aberration-corrected TEM without the panel cooling system. The image of 2,048 × 2,048 pixels was acquired with a dwell time of 3 μs, pixel size of 12.5 pm, and screen current of ~200 pA. The scanning direction is along the horizontal direction of the image as indicated by the arrow. The distortion map is measured by LADIA program. The result shows evident distortions along the scanning direction of the HAADF-STEM image resulting from environmental instabilities during imaging. c,d) Image distortion in HAADF-STEM images obtained by aberration-corrected TEM with the panel cooling system. The image of 2,048 × 2,048 pixels was acquired with a dwell time of 3 μs, pixel size of 12.5 pm, and screen current of ~200 pA. The scanning direction is indicated by the arrow. The result shows significantly reduced image distortions attributed to increased environmental stabilities during imaging.
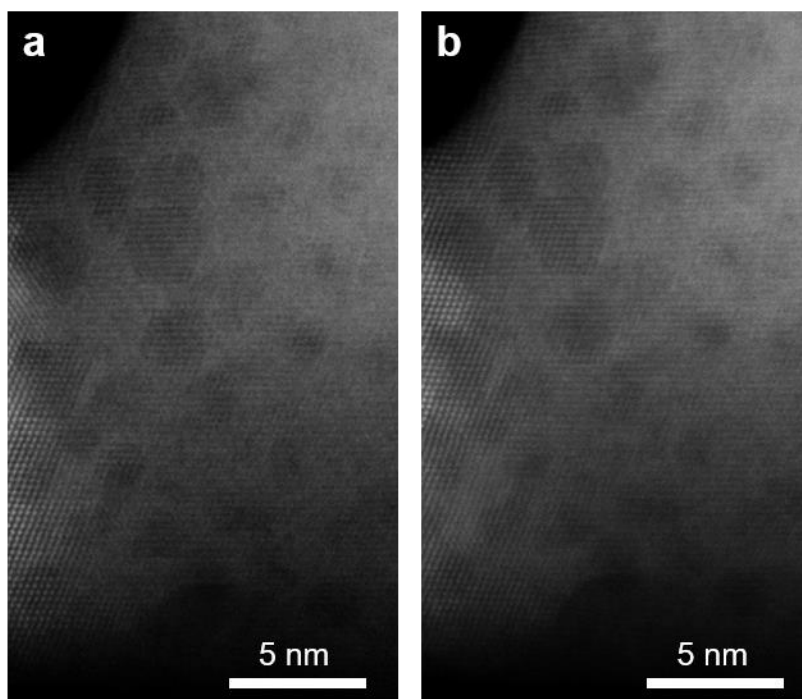
Fig. S2. Comparison of two HAADF-STEM images acquired before and after continuous high-dose beam exposure. a) Baseline image taken with a beam current of 400 pA. b) Image taken after approximately 1.5 minutes of continuous exposure under a beam current of 400pA. The supra-nano structures remain stable throughout the process.

Evaluation of the missing-wedge effect on the accuracy of the tomography

To evaluate the influence of the missing wedge on the fidelity of the atomic-resolution electron tomography and the CN analysis, we construct an atomic model of a gold nanoparticle with a total of 6522 atoms (Fig. S3a-c). Two 3D tomograms with tilt range from -90° to 90° (ground truth, GT) and from -70° to 70° (missing-wedge tomogram, MWT) were reconstructed by SIRT with a tilt interval of 2°. The tilt series were obtained by linear projection of the atomic potentials with a nonlinear factor added (Fig. S3d-f). In the reconstructed tomograms (Fig. S4a-d), the MWT indeed shows some artifacts compared to the GT, that is, the atoms (especially on the particle surface) of the MWT are slightly blurred and elongated along the x-axis (Fig. S4e-j). As a result, aside from the 6522 true atoms, 6 more atoms (e.g., the atom indicated by the arrow in Fig. S4i) are misidentified due to the artifacts in the WMT reconstructions (Fig. S5a, b, red represents ground truth atoms, and blue represents error atoms). Yet, since the intensities of these 6 misidentified atoms are evidently lower than that of the true atoms, a 3D mask based on a suitable threshold value could be used to eliminate the errors. Besides, despite the larger deviation along the x-axis introduced by the missing wedge, the mean values of the distances between adjacent atoms along <100> directions show good agreement between the GT and

MWT reconstructions (Table S1). Furthermore, based on the 3D atomic coordinates derived from the raw data and the GT and MWT reconstructions, the CNs of each atom in the model and tomograms are calculated. The CN maps obtained from the raw data, GT, and MWT reconstruction match very well (Fig. S6), and the discrepancy between the results is less than 5%. To sum up, the above evaluation confirms the reliability of the 3D reconstruction and quantitative CN analysis based on a tilt range from -75° to +75°.
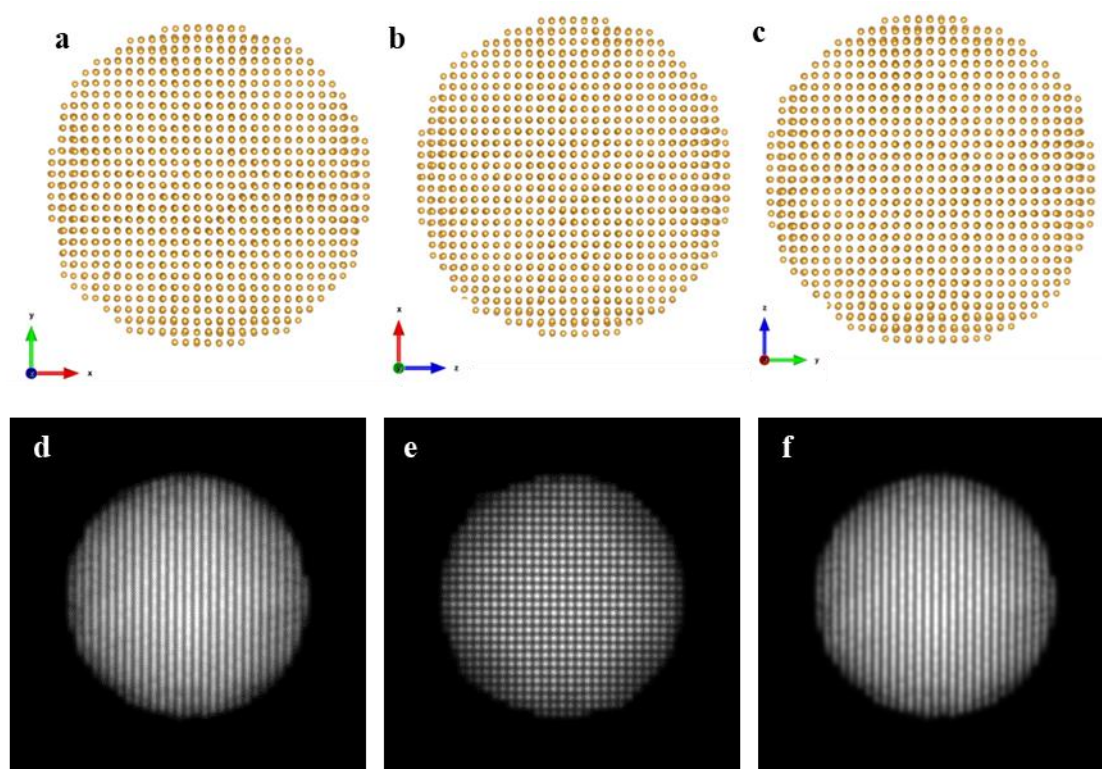

Fig. S3. The atomic model of a gold nanoparticle and three representative images of the tomographic tilt series by linearly projecting atomic potentials. a-c) 3D atomic model viewed from <100> zone axes. d-f) projections at tilt angle of -70°, 0°, and 70°, respectively.
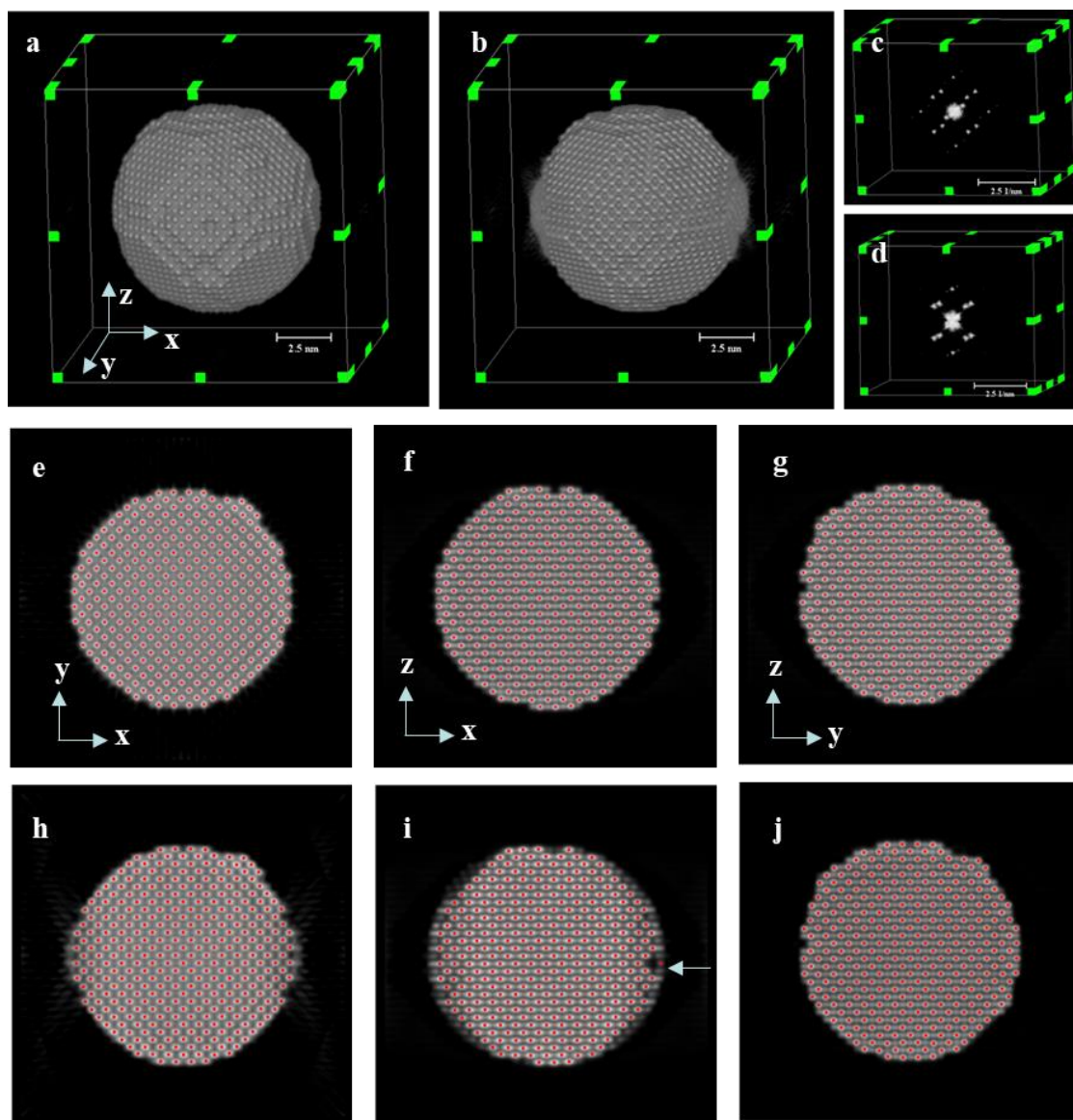
Fig. S4. Missing wedge effect on the accuracy of atomic-resolution electron tomography. a-d) The 3D reconstruction of surface structures and corresponding power spectrum obtained by GT (a and c) and MWT (b and d). Note that the x-direction is the missing wedge direction. e-j) One-atom-thick center slices perpendicular to the z-axis (e and h), y-axis (f and i), and x-axis (g and j), obtained from GT (e-g) and MWT (h-j). The red dots in the intensity maps indicate the positions of the atoms. A misidentified atom is indicated by the arrow.
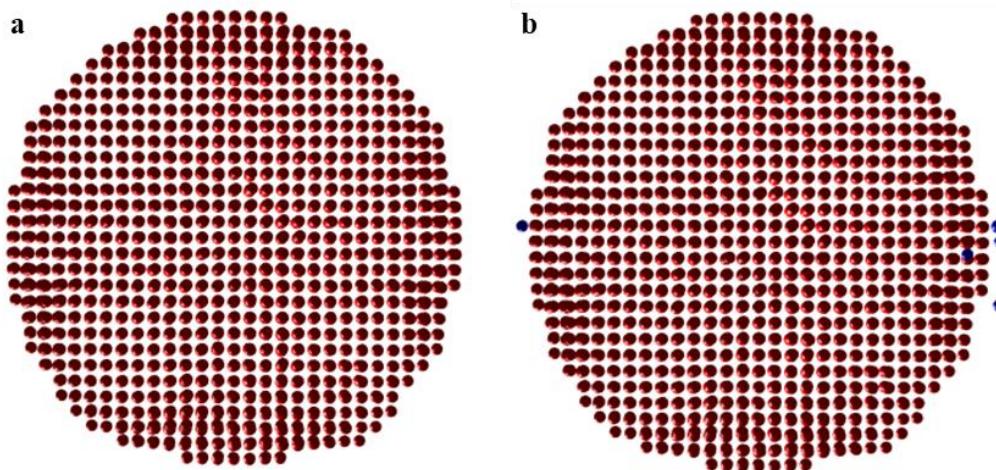
Fig. S5. 3D positions of atoms in the a) ground truth and b) MWT reconstruction. The true atoms and misidentified atoms are denoted by red and blue spheres, respectively.

Type/Direction	x-[1 0 0] (Å)	y-[0 1 0] (Å)	z-[0 0 1] (Å)
Model	4.0482	4.0488	4.0474
GT	4.0481	4.0472	4.0471
MWT	4.0473	4.0473	4.0472

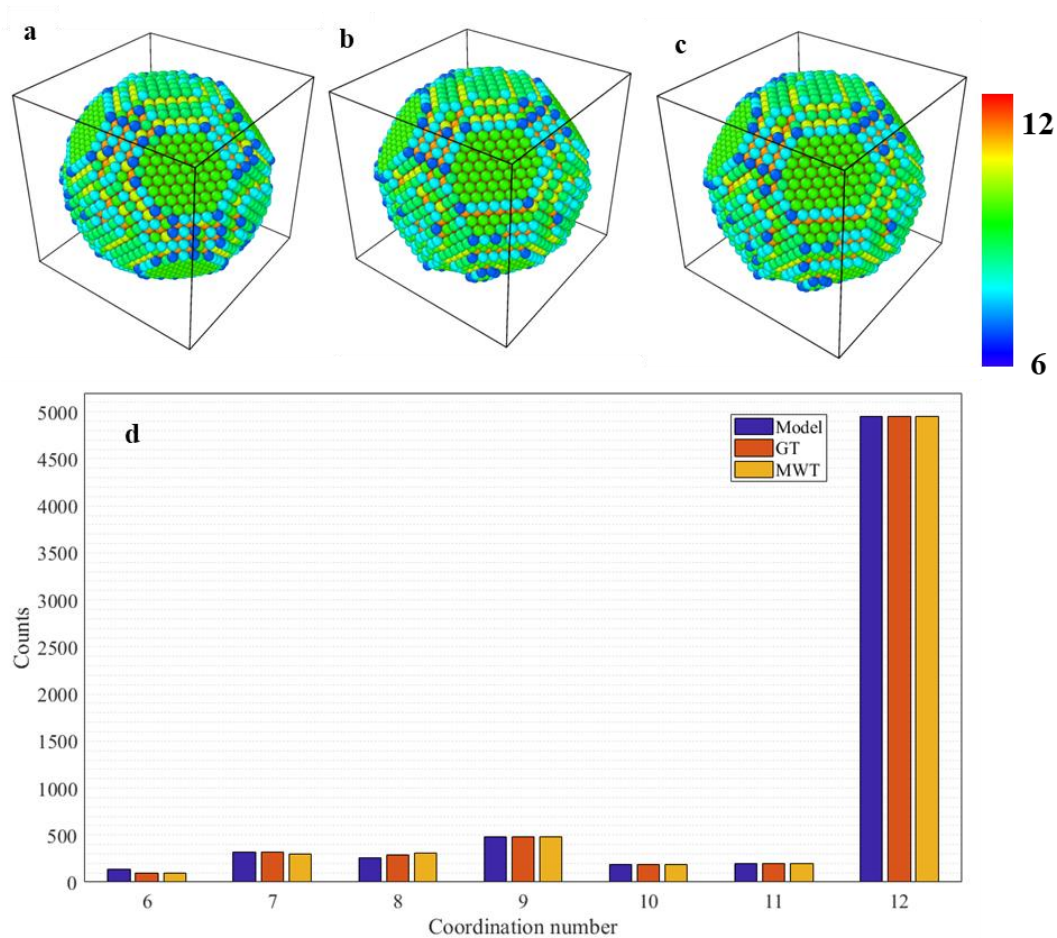**Table S1.** The mean values of distances between adjacent atoms along <100> directions.

Fig. S6. Missing wedge effect on the accuracy of coordination number (CN) determination. a-c) 3D CN maps of all the atoms in the (a) atomic model, (b) GT reconstruction, and (c) MWT reconstruction. d) Histograms of the distribution of the CNs of all the atoms obtained from (a-c).
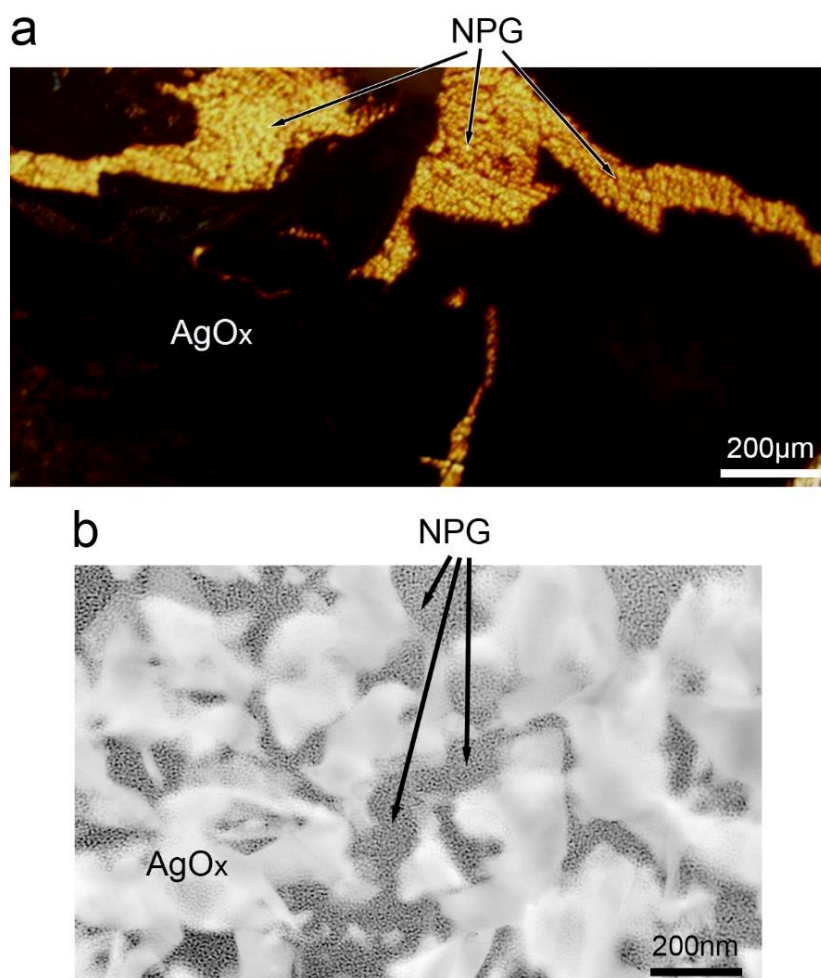
Fig. S7. AgO_x@NPG derived from thicker alloy sample. a) OM image of an AgO_x@NPG sample derived from alloy sheet with the thickness of ~300 nm. A part of the specimen surface is covered by loose AgO_x film (black color). The other region shows the color of gold, with AgO_x layer broken up and exfoliated. Note that for NPG samples used for catalytic tests, AgO_x films are completely removed by short-time ion beam etching. b) HAADF-STEM image of an AgO_x@NPG sample derived from alloy sheet with the thickness of ~300 nm. The NPG is covered with broken AgO_x layers.
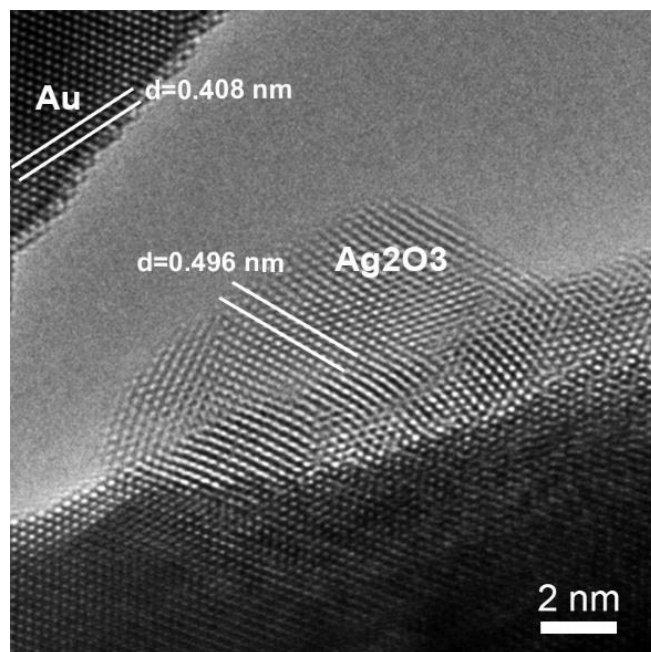
Fig. S8. AC-HRTEM image of a representative silver oxide particle on the solid-state-dealloyed NPG.
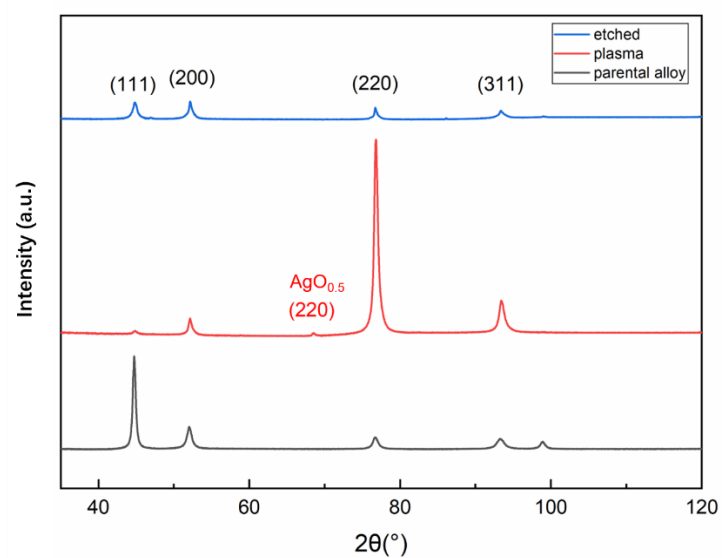

Fig. S9. XRD of the parental alloy (black), the plasma-processed sample (red), and the ion-beam etched sample (blue).
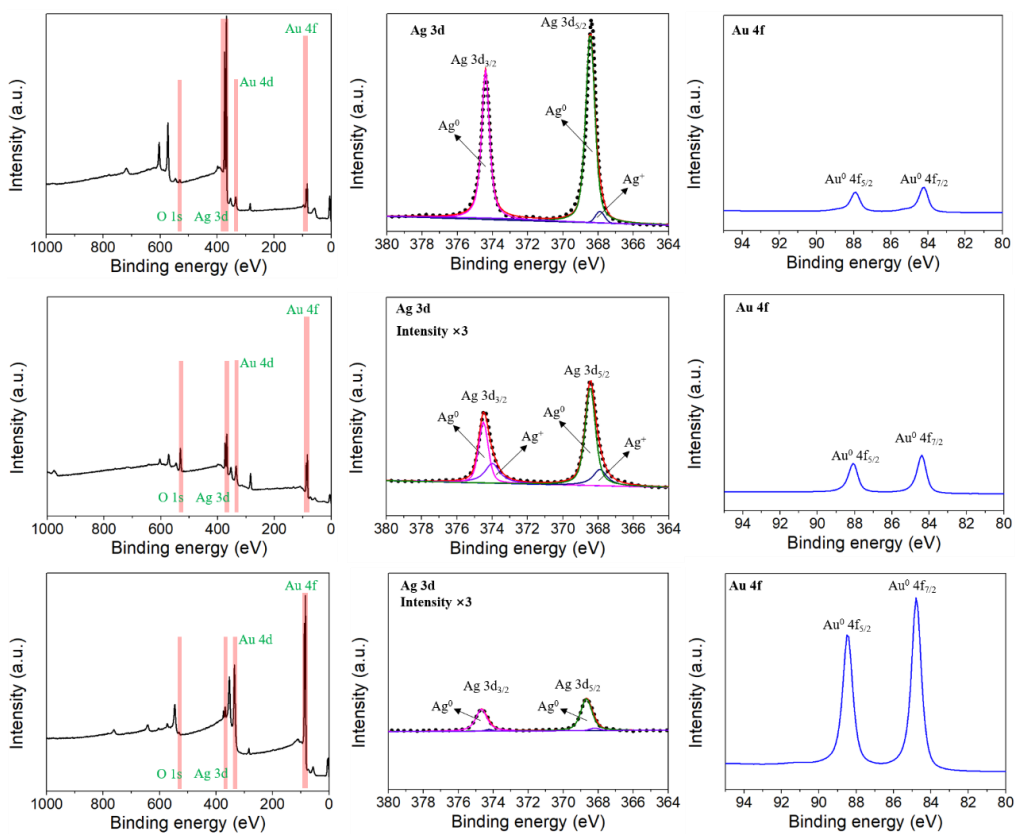
Fig. S10. XPS of the parental alloy (top panel), the plasma-processed sample (middle panel), and the ion-beam etched sample (bottom panel).

10

To demonstrate that the supra-nano surface structures are not the results of electron beam irradiation with high accelerating voltage, we first posed the beam at a sacrificial region and then captured an image right after we moved the beam to a virgin region under an accelerating voltage of 300 kV. Fig. S11a,b show aberration-corrected bright-field TEM images of solid-state-dealloyed NPG sample. The supra-nano dents or pores are evident even in very low magnification of the virgin region. In fact, we found the supra-nano dents or pores are very stable under normal AC-HRTEM imaging conditions with an accelerating voltage of 300 kV. Besides, AC-HRTEM images (Fig. S11c) were also captured in a freshly fabricated NPG sample under an accelerating voltage of 60 kV and the results show good agreement with that obtained under the accelerating voltage of 300 kV.
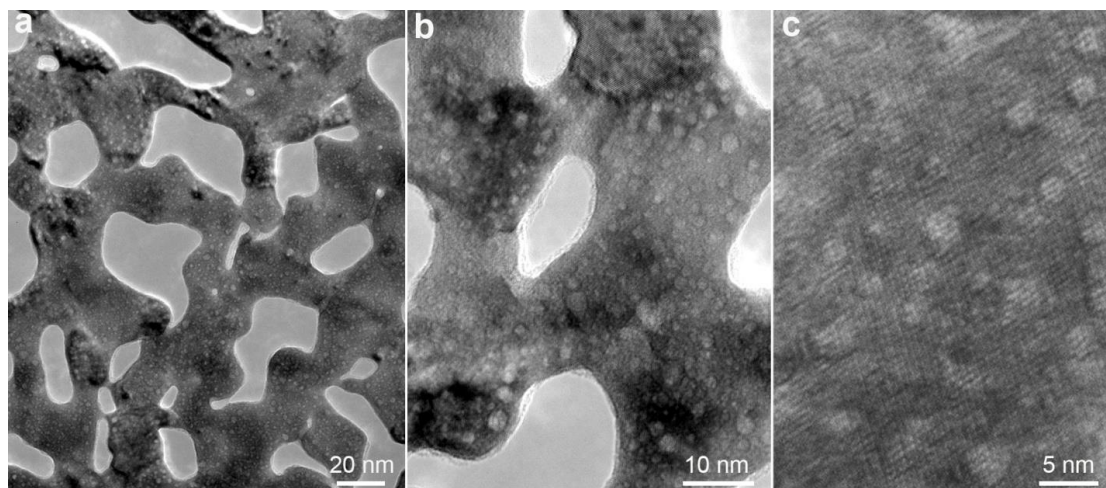

Fig. S11. TEM images of solid-state-dealloyed NPG. a) Aberration-corrected TEM image of a solid-state-dealloyed NPG specimen with supra-nano dents or pores under an accelerating voltage of 300 kV. b) AC-HRTEM image of a solid-state-dealloyed NPG specimen under an accelerating voltage of 300 kV. c) AC-HRTEM image of a virgin region in solid-state-dealloyed NPG specimen under an accelerating voltage of 60 kV.

Influence of the residual Ag in both NPGs

Ag was not completely removed from the NPGs. Since the residual Ag in the solid-state-dealloyed NPG (~5.7%, Fig. S12) is comparable to that in chemically-dealloyed NPG (~5.4%, Fig. S13), the improved catalytic performance is more likely attributed to the increased percentage of low surface coordination sites in the solid-state-dealloyed NPG.
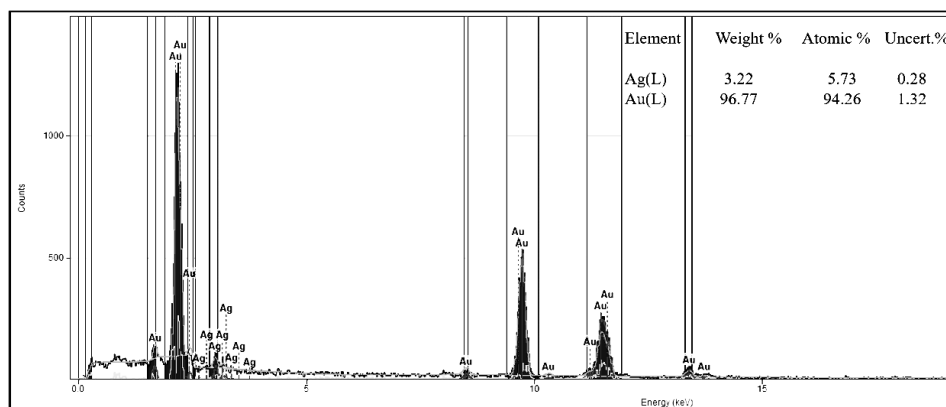

Element	Weight %	Atomic %	Uncert.%
Ag(L)	3.22	5.73	0.28
Au(L)	96.77	94.26	1.32

Fig. S12. Quantification of the residual Ag in solid-state dealloyed NPG. The EDS result was acquired by FEI Tecnai F30 TEM.

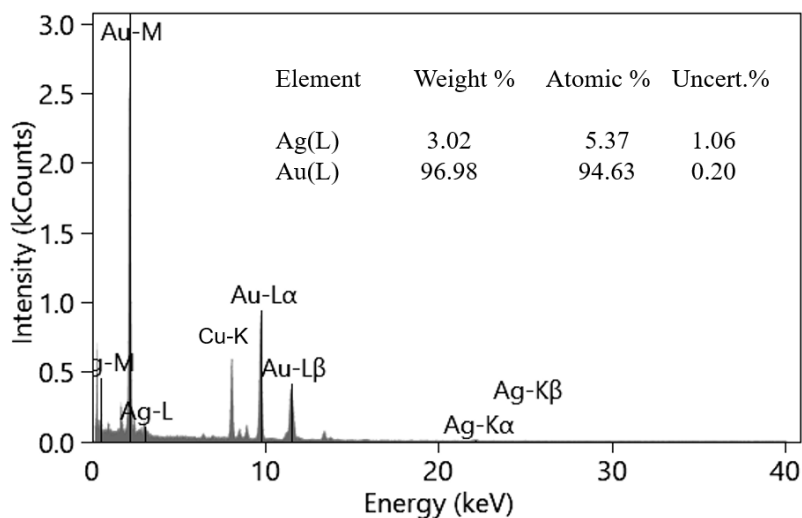| Element	Weight %	Atomic %	Uncert.%
Ag(L)	3.02	5.37	1.06
Au(L)	96.98	94.63	0.20

Fig. S13. Quantification of the residual Ag in chemically-dealloyed NPG. The EDS result was acquired by FEI Themis G^2 TEM.
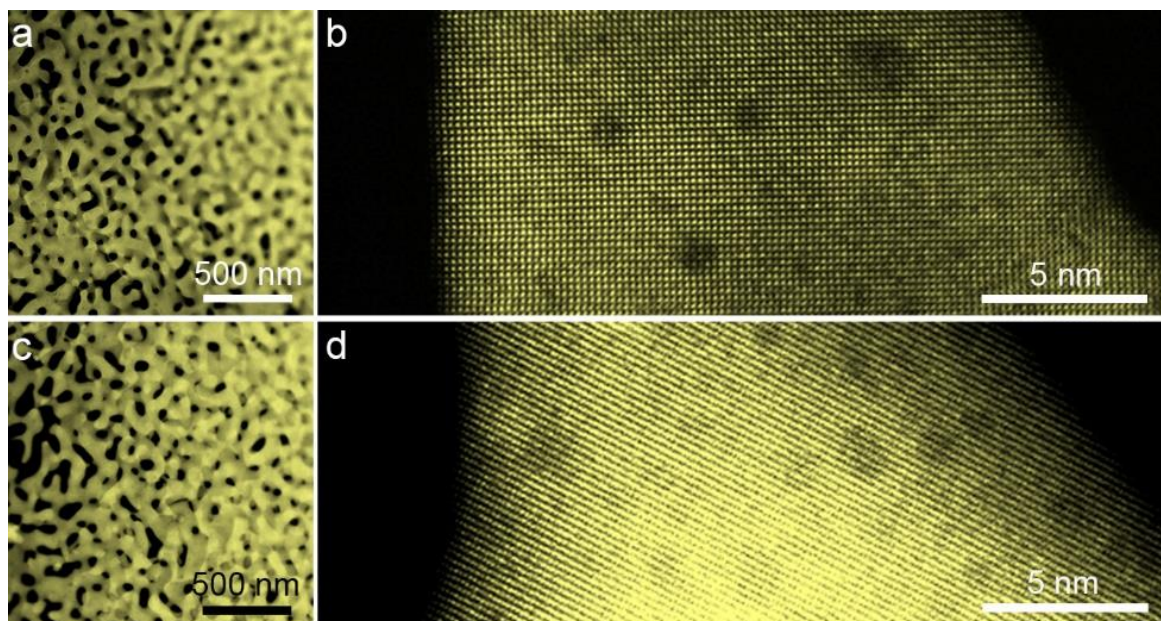
Fig. S14. Structure of solid-state-dealloyed NPG before and after CO oxidation. a,b) Low-magnification and atomic-resolution aberration-corrected HAADF-STEM image of the solid-state-dealloyed NPG specimen before CO oxidation. c,d) Low-magnification and atomic-resolution aberration-corrected HAADF-STEM image of the plasma-dealloyed NPG specimen after CO oxidation at 80 °C for 20 h.
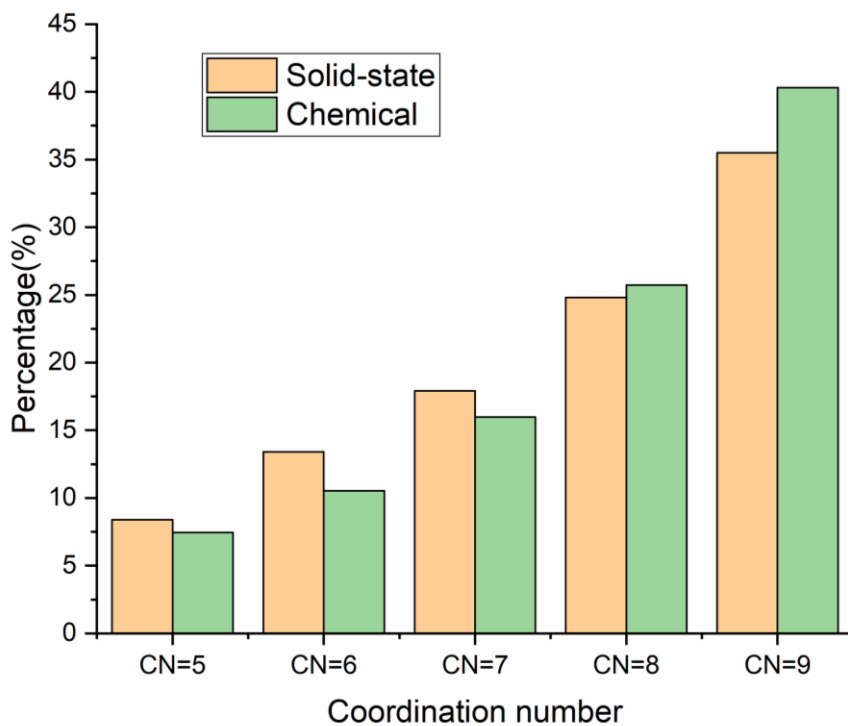
Fig. S15. Histograms showing the CN distributions of the surface atoms in chemically dealloyed NPG (green) and solid-state-dealloyed NPG (orange) with similar diameter (~9 nm).
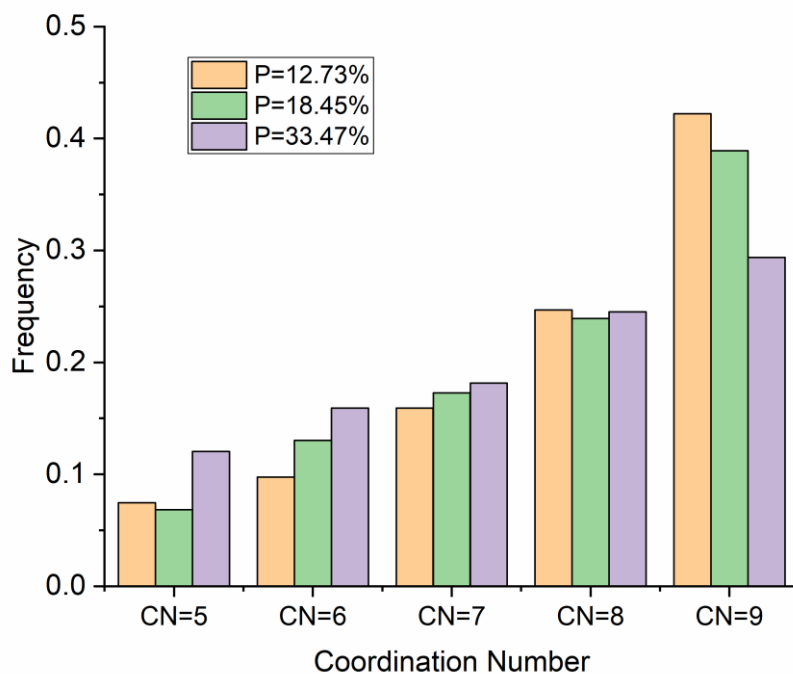

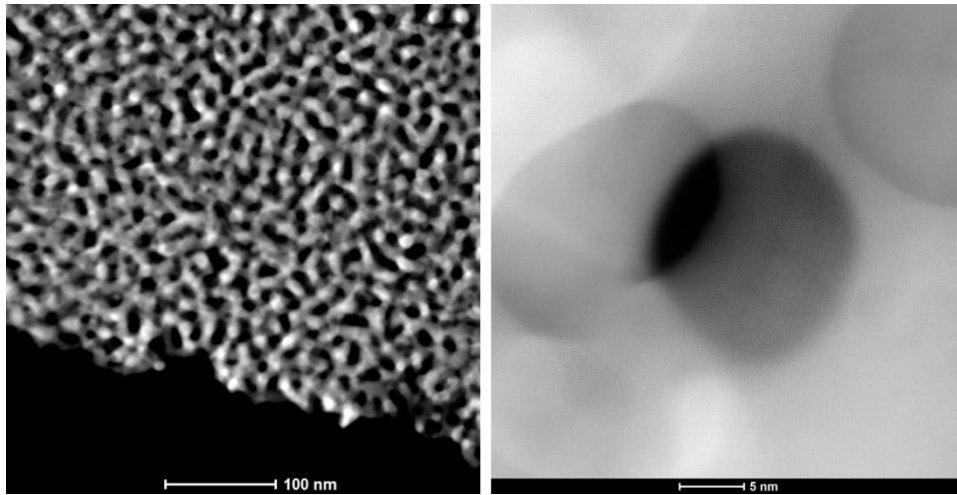**Fig. S16.** The CN distributions of solid-state-dealloyed NPG ligaments with different porosity.

Fig. S17. Morphology and atomic structure of the chemically dealloyed NPG resolved by low magnification (left) and atomic resolution (right) HAADF-STEM imaging. The NPG ligaments show smooth surface with no dents/ pores identified.